AIAA Aviation Forum and ASCEND co-located Conference Proceedings
29 July - 2 August 2024, Las Vegas, Nevada
AIAA AVIATION FORUM AND ASCEND 2024

10.2514/6.2024-4653

Time-Domain System Identification and Validation of Small Fixed-Wing UAV Dynamics

Bogdan Løw-Hansen [*], Richard Hann[†], and Tor Arne Johansen[‡]
Norwegian University of Science and Technology, NTNU, Trondheim, 7491, Norway

Christoph Deiler[§]
DLR (German Aerospace Center), Braunschweig, 38108, Germany

This paper presents time domain identification and validation of the aerodynamic model of the Skywalker X8 unmanned aerial vehicle (UAV). Previous modeling efforts include static coefficients derived from wind tunnel experiments and a model based on body velocity coefficients. Our study builds on these results, introducing a new model that adheres to the classical aerodynamic structure identified through stepwise regression. Our paper combines propulsion system modeling results based on wind tunnel tests with data from flight experiments to identify the airframe aerodynamics of the Skywalker X8 UAV. To validate the model, we present model predictions for 10-second long maneuvers, performed at the cruise speed of 18 m/s, including force and moment coefficients (C_D, C_Y, C_L, C_l, C_m, C_n). In summary, this paper introduces a novel simulation-ready aerodynamic model for the Skywalker X8 UAV, identified in the stability frame, allowing a direct comparison with a larger set of UAV models and CFD results available in the literature, often presented in terms of lift and drag analysis.

Nomenclature

h = Altitude , m
m = Aircraft mass , kg
g = Gravitiational acceleration , m/s^2
ρ = Air density , kg/m^3
$\bar{q}$ = Dynamic pressure , Pa
V_a = Airspeed , m/s
α = Angle of attack , rad
β = Sideslip , rad
γ = Flight path angle , rad
x, y, z = Body-axis position coordinates , m
ϕ, θ, ψ = Roll, Pitch, Yaw angles , rad
u, v, w = Body-axis linear velocities , m/s
u_a, v_a, w_a = Aerodynamic system velocities , m/s
p, q, r = Body-axis angular velocitites , rad/s
p^*, q^*, r^* = nondimensional angular velocitites
a_x, a_y, a_z = Body-axis linear accelerations , m/s^2
$\delta_\mathrm{e}, \delta_\mathrm{a}$ = Elevator and Aileron deflection , rad
δ_r = Rudder deflection , rad
δ_t = Throttle command normalized $\in$ [0,1]
δ_{er}, δ_{el} = Right and left elevon deflections , rad
C_X, C_Y, C_Z = Body-axis force coefficients
C_l, C_m, C_n = Body-axis moment coefficients
C_D, C_L = Drag and lift coefficients
C_T, C_Q = Propeller thrust and torque coefficients
$\boldsymbol{F}$ = Aircraft force vector , N
$\boldsymbol{M}$ = Aircraft moment vector , Nm
$\boldsymbol{f}$ = Specific force vector , m/s^2
$\boldsymbol{h}_p$ = Propeller angular momentum kgm^2/s
$\boldsymbol{I}$ = Aircraft inertia matrix
$I_{\{x,y,z,xz\}}$ = Aircraft moments of inertia , kgm^2
I_p = Propeller moment of intertia , kgm^2
J = Advance ratio
Ω_p = Rotational motor speed , rad/s
T = Propeller thrust , N
Q = Propeller torque , Nm
D = Propeller diameter , m
R = Electric motor resistance , Ω
K_E = Back-emf constnat , V/(rad/s)
U_b = Power supply (battery) voltage , V
I_b = Power supply (battery) current , A
U = Motor voltage , V
I_m = Motor current , A
Q_m = Motor torque , Nm
P_{el}, P_m = Electrical and mechanical motor power, W
P_b = Power supply (battery) power, W
S = Planform area of the wing , m^2

---

[*] PhD-candidate, NTNU, Department of Engineering Cybernetics. Corresponding author email: bogdan.l.hansen@ntnu.no
[†] Senior Researcher, NTNU, Department of Engineering Cybernetics. Corresponding author email: richard.hann@ntnu.no
[‡] Professor, NTNU, Department of Engineering Cybernetics, tor.arne.johansen@ntnu.no
[§] Research Scientist, Institute of Flight Systems, Braunschweig, christoph.deiler@dlr.de

$\bar{c}$ = Mean aerodynamic chord , m
b = Wingspan , m
$\boldsymbol{r}$ = Distance vector , m
$\boldsymbol{p}$ = Position vector , m
$\boldsymbol{v}$ = Linear velocity vector , m/s
$\boldsymbol{\omega}$ = Angular rate vector , rad/s
$\boldsymbol{R}$ = SO(3) rotation matrix
{i} = Inertial frame
{n} = North-East-Down (NED) frame
{b} = Body frame
{s} = Stability frame
{w} = Wind frame
$\{m_I\}$ = Sensor frame
$\widehat{\ }$ = Hat indicates model prediction results
$_w$ = Wind velocity subscript
$_a$ = Relative velocity subscript

Abbreviations

CFD computational fluid dynamics
CG center of gravity
DOF degree-of-freedom
EKF extended Kalman filter
GNC guidance, navigation, and control
GNSS global navigation satellite system
IMU inertial measurement unit
NED North-East-Down
OEM output error method
UAV unmanned aerial vehicle

I. Introduction

It is clear that by 2024, small, cost-effective unmanned aerial vehicles (UAVs), also known as UAS, RPAS, or simply drones, have transcended their niche hobby and research applications to become an integral part of various industry and defense sectors [1, 2]. Although professional users find these platforms robust enough for many of their applications, the increase in use has revealed many limitations related to the operation of small UAVs in real-world scenarios; among the most challenging issues concern operations in harsh weather conditions [3, 4]. One way to approach these challenges is through simulation-based testing and development. A high-fidelity model and a simulator framework make it possible to test and develop guidance, navigation, and control (GNC) algorithms capable of handling various adverse conditions without risking losing the aircraft while it is in the air. We aim to facilitate this simulation-based approach by presenting the model development process and the identified aerodynamic parameters of the Skywalker X8 UAV, used as a case study in this article. The Skywalker X8 UAV is a small flying wing controlled by two elevons and a rear-mounted propeller as shown in Fig. 1. The physical properties of the aircraft are shown in Table 1.

Fig. 1 Skywalker X8 UAV

Table 1 Physical properties of the Skywalker X8 UAV.

Property	Value
m	3.364 kg
I_x	0.335 kgm^2
I_y	0.140 kgm^2
I_z	0.400 kgm^2
I_{xz}	0.029 kgm^2
$\bar{c}$	0.36 m
b	2.10 m
S	0.75 m^2

Our paper contributes a novel model of the Skywalker X8 UAV. However, previous modeling efforts have been made, such as [5], where the authors focused on identifying static aerodynamic coefficients based on wind tunnel experiments, and [6], where the authors extended the results through system identification experiments to identify velocity-based parameters. Although the velocity-based model in [6] provides valuable information on the dynamics of the aircraft, it is not easily comparable to most other models available in the literature. There are two main reasons for this: firstly, the model in [6] has a complex structure with a high number of parameters and nonlinear regressors; secondly, the model is identified in the body frame, as opposed to the stability frame used in the classical system identification approaches [7, 8]. Furthermore, the model coefficients identified in the stability frame are more convenient to compare against the results based on computational fluid dynamics (CFD), which are presented primarily in terms of the lift and drag curves. This is particularly relevant in the case of aircraft icing research, where a considerable amount of data has been accumulated on the change of lift and drag coefficients as a function of ice accretion [9–15]. Consequently, to allow for convenient validation and comparison with available research, the aerodynamic model presented in this paper was identified in the stability frame. The system identification process was performed following the classical time-domain methodology described in [7, 8], which was greatly simplified by the access to the DLR's (German Aerospace Center) system identification tool Fitlab [16].

In the past decade, numerous research groups have successfully conducted system identification of aerodynamic models for small fixed-wing UAV platforms [5, 6, 17–26]. These models include longitudinal and lateral dynamics models, with parameters identified in both body and stability frames. Although invaluable for simulation-aided testing and development of UAVs, the diverse range of modeled platforms, variations in modeling assumptions, and use-case-specific adaptations mean that the available models do not always align with the needs of subsequent users. This paper aims to address this challenge by contributing to the set of validated small fixed-wing UAV models, thus offering users a wider selection to better match their specific application requirements.

In summary, this paper presents a comprehensive study on the modeling and identification of a 6-degree-of-freedom (DOF) aerodynamic model based on the Skywalker X8 UAV platform. Our final model comprises 44 coefficients distributed among the aerodynamic, propulsion, and servo models. The presentation and analysis of the model prediction results are done with the primary objective of enabling high-fidelity simulation testing using the identified models.

II. Methods

This section includes the theory necessary to set up and perform system identification based on the time domain output error method (OEM) [7, Chap. 6.2]. More specifically, this concerns the transformation of sensor measurement from sensor frame to center of gravity (CG), propulsion force and moment calculations, aerodynamic system modeling, and simulation. The theory related to the optimization solver used by the OEM is considered to be outside of the scope of this paper and is therefore not included; if necessary, the relevant information can be found in [8, 16].

There are many ways to express vectors and rotations. In this paper, the notation from [27] is adopted. An example of vectors and a rotation between the body frame {b} and North-East-Down (NED) frame {n} is presented here, where the NED frame is considered inertial:

$\boldsymbol{v}_{nb}^{b}$ — linear velocity of the body frame origin relative to the NED origin, expressed in {b},
$\boldsymbol{v}_{nb}^{n}$ — linear velocity of the body frame origin relative to the NED origin, expressed in {n},
$\boldsymbol{\omega}_{nb}^{b}$ — angular velocity of {b} relative to {n}, expressed in {b},
$\boldsymbol{R}_{b}^{n}$ — SO(3) rotation matrix that takes a vector from {b} to {n}.

A. Sensor Measurement Transformations

When working with aircraft dynamics and kinematics, the time derivative of a vector in a rotating reference frame has to be defined. In Eq. (1) let ${}^{i}\mathrm{d}/\,\mathrm{d}t$ denote the time differentiation in the inertial frame {i}, and ${}^{b}\mathrm{d}/\,\mathrm{d}t$ in the body frame {b}. The time derivative of a vector $\vec{(\cdot)}$ in a rotating reference frame {b}, expressed in the body frame {b}, has two parts; (i) a part that accounts for the rate of change of the vector in the rotating reference frame {b} and (ii) a part that accounts for the rotation of the axis of the reference frame {b} in the inertial frame {i}, denoted by $\boldsymbol{\omega}_{ib}$ [27, Chap. 3.1].

$$\frac{{}^{i}\mathrm{d}}{\mathrm{d}t}\vec{(\cdot)} = \frac{{}^{b}\mathrm{d}}{\mathrm{d}t}\vec{(\cdot)} + \boldsymbol{\omega}_{ib} \times \vec{(\cdot)} \tag{1}$$

Moreover, the location of the body frame origin with respect to the aerodynamic center and the CG has to be defined. For Skywalker X8, the origin of the body frame $\{b\}$ is placed in the aerodynamic center which is assumed to coincide with the nominal CG of the UAV, such that the vector from the origin of $\{b\}$ to CG in the body frame is

$\boldsymbol{r}^b_{bCG} = [0, 0, 0]^\top$. This simplifying assumption is reasonable when the CG is not expected to change during flight and the distance between the aerodynamic center and CG is small. Depending on the UAV, the aerodynamic center and the CG might be far apart. The validity of the assumption must, therefore, be assessed separately for each platform. Otherwise, the location of the aerodynamic center with respect to CG must be taken into account when computing the aerodynamic moments, as shown in [8, Eq. (6.75)].

In a moving vehicle, measurements of acceleration and estimates of linear velocity change based on the location of the sensors, e.g., the inertial measurement unit (IMU), in the vehicle. It is, therefore, necessary to transform the IMU measurement from the sensor frame $\{m_I\}$ to the aircraft CG to get the correct reading of the aircraft's movement. The transformation can be done based on the distance vector that specifies the location of the sensor frame $\{m_I\}$ with respect to CG:

$$\boldsymbol{r}^b_{m_I CG} = \boldsymbol{r}^b_{bCG} - \boldsymbol{r}^b_{bm_I} = \begin{bmatrix} x_{CG} - x_{m_I} \\ y_{CG} - y_{m_I} \\ z_{CG} - z_{m_I} \end{bmatrix} . \tag{2}$$

The velocities in the flight experiment data $\boldsymbol{v}^b_{nm_I}$ are the output of an extended Kalman filter (EKF) located in the sensor frame and, therefore, must be transformed from the sensor frame to CG. Following [27, Chap. 14], the transformation can be performed in the following way:

$$\boldsymbol{v}^b_{nb} = \boldsymbol{v}^b_{nm_I} + \boldsymbol{\omega}^b_{nb} \times \boldsymbol{r}^b_{m_I CG} \quad , \quad \boldsymbol{v}^b_{nb} = \begin{bmatrix} u \\ v \\ w \end{bmatrix} \quad , \quad \boldsymbol{\omega}^b_{nb} = \begin{bmatrix} p \\ q \\ r \end{bmatrix} . \tag{3}$$

Similarly, the accelerations measured by the IMU in the sensor frame $\boldsymbol{f}^b_{nm_I}$ have to be transformed to CG. The transformation is derived by time differentiation of Eq. (3):

$$\boldsymbol{f}^b_{nb} = \boldsymbol{f}^b_{nm_I} + \dot{\boldsymbol{\omega}}^b_{nb} \times \boldsymbol{r}^b_{m_I CG} + \boldsymbol{\omega}^b_{nb} \times (\boldsymbol{\omega}^b_{nb} \times \boldsymbol{r}^b_{m_I CG}) . \tag{4}$$

B. Propulsion System Modeling

The Skywalker X8 UAV is driven by a pusher propeller located behind the fuselage. When the propeller rotates, it generates a thrust, which pushes the UAV forward, and a roll moment, which the motor has to match to sustain the desired motor speed. Additionally, the propeller generates a gyroscopic moment, which resists deviation from its rotation axis. The generated roll moment is mainly due to drag and friction associated with propeller rotation, while the gyroscopic moment is caused by the rotating mass of the propeller and the motor shaft. Modeling of the drag-related roll moment is described in [28, Chap. 4.3] while the gyroscopic effect model can be found in [7, Chap. 3.2]. In general, the gyroscopic effect is often neglected as it is an order of magnitude smaller than the total torque, although it can become significant when the rotating mass is large enough. The propeller torque model should, therefore, be based on the available data and model requirements.

The propeller thrust T and torque Q in Eqs. (5) and (6) are modeled as functions of the airspeed V_a, the motor speed Ω_p, and the advance ratio J defined in Eq. (7). The effects of the Reynolds and the Mach numbers are omitted as they are not as significant at slow speeds [29–31], which is the operational envelope of interest for small fixed-wing UAVs.

$$Q = \frac{\rho D^5}{4\pi^2} C_Q(J) \Omega_p^2 \tag{5}$$

$$T = \frac{\rho D^4}{4\pi^2} C_T(J) \Omega_p^2 \tag{6}$$

$$J = \frac{2\pi V_a}{\Omega_p D} \tag{7}$$

In this work, based on modeling results presented later in Section III, the torque and thrust coefficients C_Q, C_T are modeled as second- and third-order polynomials of J:

$$C_Q(J) = C_{Q_0} + C_{Q_1} \cdot J + C_{Q_2} \cdot J^2 \tag{8}$$

$$C_T(J) = C_{T_0} + C_{T_1} \cdot J + C_{T_2} \cdot J^2 + C_{T_3} \cdot J^3 \ . \tag{9}$$

The gyroscopic propeller moment, $\boldsymbol{M}^b_{prop,gyro}$ generated by the rotating mass in the body axis is computed as a function of the propeller inertia I_p, and the motor speed Ω_p,

$$\boldsymbol{h}_p = \begin{bmatrix} I_p\Omega_p \\ 0 \\ 0 \end{bmatrix} . \tag{10}$$

The reference frame where the torque is applied is rotating with respect to the inertial frame. The gyroscopic propeller torque is therefore defined according to Eq. (1), verified in [7, Chap. 3.2]:

$$\boldsymbol{M}^b_{prop,gyro} = I_p\dot{\boldsymbol{h}} + \boldsymbol{\omega}^b_{nb} \times I_p\boldsymbol{h} = \begin{bmatrix} I_p\dot{\Omega}_p \\ 0 \\ 0 \end{bmatrix} + \begin{bmatrix} 0 \\ I_p\Omega_p r \\ -I_p\Omega_p p \end{bmatrix} = \begin{bmatrix} I_p\dot{\Omega}_p \\ I_p\Omega_p r \\ -I_p\Omega_p p \end{bmatrix} . \tag{11}$$

The total propeller torque can, therefore, be modeled as follows,

$$\boldsymbol{M}_{prop} = \begin{bmatrix} Q \\ 0 \\ 0 \end{bmatrix} + \boldsymbol{M}^b_{prop,gyro} \ . \tag{12}$$

The sign of the produced torque depends on the direction of rotation and location of the propeller with respect to CG. For a clockwise rotating propeller mounted at the front of the aircraft along the aircraft's x-axis, the produced torque is positive w.r.t. body fixed axes. For a propeller mounted in the rear, like on the Skywalker X8 UAV, the produced propeller torque is negative, leading to the following definition:

$$\boldsymbol{M}_{prop,rear} = -\boldsymbol{M}_{prop} \ . \tag{13}$$

C. Aerodynamic Modeling and Simulation

This section presents the equations of motion and other relevant relations needed to simulate the UAV dynamics and reproduce the measured flight data.

1. Flying Wing Configuration

The aerodynamic modeling of an aircraft is highly affected by its geometry and control surface configuration. The Skywalker X8 UAV is a flying wing platform with two control surfaces — right and left elevons (δ_{er}, δ_{el}), normally specified in radians. In this configuration, the elevons replace the function of the elevator and the aileron ($\delta_\mathrm{e}, \delta_\mathrm{a}$), which are the standard control inputs used in aerodynamic modeling. Driving the elevons together emulates the elevator command while driving them differentially emulates the aileron command. Mathematically, the transformation from elevons to elevator and aileron is defined as follows:

$$\begin{bmatrix} \delta_\mathrm{e} \\ \delta_\mathrm{a} \end{bmatrix} = \frac{1}{2} \begin{bmatrix} 1 & 1 \\ -1 & 1 \end{bmatrix} \begin{bmatrix} \delta_{er} \\ \delta_{el} \end{bmatrix} . \tag{14}$$

Furthermore, the platform has no rudder, so the rudder input δ_r is not used. Instead, the Skywalker X8 has blended winglets to provide directional stability, as seen in Fig. 1. The propulsion on the Skywalker X8 platform is achieved through a single rear-mounted propeller, controlled by a throttle input $\delta_t \in [0, 1]$.

2. Modeling Aerodynamic Forces and Moments

Modeling and dynamic system simulation are crucial components of the output-error-based system identification method. More specifically, the OEM requires the computation of system dynamics based on a set of model parameters that can be updated iteratively during the identification process. This way, the model parameters can be adjusted to minimize the discrepancy between the simulated model output and the measured experiment data.

Computation of the aerodynamic forces and moments starts with the aerodynamic state of the aircraft, i.e., the airspeed V_a, the angle of attack α, and the sideslip angle β. The aerodynamic state can be derived from the inertial and wind velocities as shown in Eqs. (15) and (16).

$$\begin{bmatrix} u_a \\ v_a \\ w_a \end{bmatrix} = \begin{bmatrix} u - u_w \\ v - v_w \\ w - w_w \end{bmatrix} \tag{15}$$

$$V_a = \sqrt{u_a^2 + v_a^2 + w_a^2} \quad , \quad \alpha = \tan^{-1}\left(\frac{w_a}{u_a}\right) \quad , \quad \beta = \sin^{-1}\left(\frac{v_a}{V_a}\right) \ . \tag{16}$$

Given the aerodynamic state of the aircraft, the generated forces and moments can be computed. The exact relation depends on the model structure, normally given as a set of polynomial equations [7]. The selection of the model structure is part of the system identification process. In this study, the selection was initially based on previous modeling results for similar UAV platforms [23, 24, 26] and then verified using the stepwise regression algorithm described in [7, Chap. 5], resulting in the following aerodynamic model structure:

$$C_L = C_{L_0} + C_{L_\alpha}\alpha + C_{L_q} q^* + C_{L_{\delta_\mathrm{e}}}\delta_\mathrm{e} \tag{17a}$$

$$C_D = C_{D_0} + C_{D_q} q^* + C_{D_{C_T}} C_T + C_{D_{k1}} C_L + C_{D_{k2}} C_L^2 \tag{17b}$$

$$C_m = C_{m_0} + C_{m_\alpha}\alpha + C_{m_q} q^* + C_{m_{\delta_\mathrm{e}}}\delta_\mathrm{e} \ , \tag{17c}$$

$$C_Y = C_{Y_0} + C_{Y_\beta}\beta + C_{Y_p} p^* + C_{Y_r} r^* + C_{Y_{\delta_\mathrm{a}}}\delta_\mathrm{a} \tag{18a}$$

$$C_l = C_{l_0} + C_{l_\beta}\beta + C_{l_p} p^* + C_{l_r} r^* + C_{l_{\delta_\mathrm{a}}}\delta_\mathrm{a} \tag{18b}$$

$$C_n = C_{n_0} + C_{n_\beta}\beta + C_{n_p} p^* + C_{n_r} r^* + C_{n_{\delta_\mathrm{a}}}\delta_\mathrm{a} \ , \tag{18c}$$

where $\delta_\mathrm{e}, \delta_\mathrm{a}, \delta_t$ are the elevator, aileron and throttle control commands and $[p^*, q^*, r^*]$ are the nondimensional angular rates normalized by airspeed and wing size, i.e., the wingspan b and the mean aerodynamic chord length $\bar{c}$:

$$p^* = \frac{pb}{2V_a} \quad , \quad q^* = \frac{q\bar{c}}{2V_a} \quad , \quad r^* = \frac{rb}{2V_a} \ ,$$

Due to its low weight and large surface area, the Skywalker X8 UAV is highly susceptible to wind gusts. During the flight experiments, the UAV encountered strong winds, which impacted the overall quality of the measured data. Consequently, to ensure the model does not overfit the data, low complexity and compatibility with similar research were weighted to a greater degree in the modeling process. The aerodynamic model in Eqs. (17) and (18) is almost linear, except for the drag equation, where the nonlinearities are introduced in thrust and lift regressors. Moreover, the model is decoupled along the longitudinal-lateral axes. Although the actual dynamics are likely coupled, and the stepwise regression results suggested that sideslip explains some of the variations in lift and drag, the overall model prediction error was not improved by including sideslip in the longitudinal model.

3. Stability to Body Frame Transformation

The lift and drag forces in Eq. (17) are generated in the stability frame. However, when simulating the aircraft dynamics, it is useful to compute these forces in the body frame. This way, the total force acting on the aircraft, consisting of the aerodynamic, propulsive, and gravitational components, can be more easily computed.

Starting from the stability frame coefficients (C_D, C_L), the body frame coefficients (C_X, C_Z) can be acquired by a change of direction and a rotation $\boldsymbol{R}_b^{s\top}$ through the angle of attack α. The rotation matrix is defined as follows:

$$\boldsymbol{R}_b^s(\alpha) = \begin{bmatrix} \cos(\alpha) & 0 & \sin(\alpha) \\ 0 & 1 & 0 \\ -\sin(\alpha) & 0 & \cos(\alpha) \end{bmatrix} \tag{19}$$

and the transformation is then computed as,

$$\begin{bmatrix} C_X \\ C_Y \\ C_Z \end{bmatrix} = \boldsymbol{R}_b^{s\top}(\alpha) \begin{bmatrix} -C_D \\ C_Y \\ -C_L \end{bmatrix} . \tag{20}$$

Given C_X and C_Z, the aerodynamic forces in the body frame $\boldsymbol{F}_{aero}^b$ can finally be computed:

$$\boldsymbol{F}_{aero}^b = \bar{q}S \begin{bmatrix} C_X \\ C_Y \\ C_Z \end{bmatrix} , \tag{21}$$

where $\bar{q} = \frac{1}{2}\rho V_a^2$ is the dynamic pressure. Computation of the aerodynamic moments $\boldsymbol{M}_{aero}^b$ and the propulsion force $\boldsymbol{F}_{prop}^b$ can be done directly in the body frame while the gravity force has to be transformed from NED to body:

$$\boldsymbol{M}_{aero}^b = \bar{q}S \begin{bmatrix} bC_l \\ \bar{c}C_m \\ bC_n \end{bmatrix} \quad , \quad \boldsymbol{F}_{prop}^b = \begin{bmatrix} T \\ 0 \\ 0 \end{bmatrix} \quad , \quad \boldsymbol{F}_{gravity}^b = \boldsymbol{R}_b^{n\top} \begin{bmatrix} 0 \\ 0 \\ mg \end{bmatrix} ,$$

where $\boldsymbol{R}_b^n$ is the body to NED rotation matrix.

With all components computed in the body frame, the total forces $\boldsymbol{F}$ and moments $\boldsymbol{M}$ can be put together as follows:

$$\boldsymbol{F}^b = \boldsymbol{F}_{aero}^b + \boldsymbol{F}_{prop}^b + \boldsymbol{F}_{gravity}^b \tag{22a}$$

$$\boldsymbol{M}^b = \boldsymbol{M}_{aero}^b + \boldsymbol{M}_{prop}^b . \tag{22b}$$

4. Simulation

Dynamic system simulation involves iteratively calculating forces and moments based on the system's dynamic state at each time step. These calculated forces and moments are then used to compute linear and angular velocities, as well as the system's position and attitude. The output of each iteration provides the system's new dynamic state, which serves as the input for computing forces and moments in the next time step.

In dynamic simulations, we typically establish the starting point within an inertial world frame, such as the NED frame. To describe the motion of a rotating body within this inertial frame, we rely on Newton's second law of motion:

$$\boldsymbol{F}^b = m\left(\dot{\boldsymbol{v}}_{nb}^b + \boldsymbol{\omega}_{nb}^b \times \boldsymbol{v}_{nb}^b\right) \tag{23a}$$

$$\boldsymbol{M}^b = \boldsymbol{I}\dot{\boldsymbol{\omega}}_{nb}^b + \boldsymbol{\omega}_{nb}^b \times \boldsymbol{I}\boldsymbol{\omega}_{nb}^b , \tag{23b}$$

where $\boldsymbol{I}$ is the inertia matrix. For aircraft, the moments of inertia are often assumed symmetric about the body x-z plane such that $I_{xy} = I_{yz} = 0$ [28], resulting in:

$$\boldsymbol{I} = \begin{bmatrix} I_x & 0 & -I_{xz} \\ 0 & I_y & 0 \\ -I_{xz} & 0 & I_z \end{bmatrix} . \tag{24}$$

With body frame forces and moments available from Eqs. (22a) and (22b), Newton's second law of motion can be reformulated to compute updates of the linear and angular accelerations:

$$\dot{\boldsymbol{v}}^b_{nb} = \frac{1}{m}\boldsymbol{F}^b - \boldsymbol{\omega}^b_{nb} \times \boldsymbol{v}^b_{nb} \tag{25a}$$

$$\dot{\boldsymbol{\omega}}^b_{nb} = \boldsymbol{I}^{-1}\left(\boldsymbol{M}^b - \boldsymbol{\omega}^b_{nb} \times \boldsymbol{I}\boldsymbol{\omega}^b_{nb}\right) . \tag{25b}$$

and based on $\boldsymbol{v}^b_{nb}$ and $\boldsymbol{\omega}^b_{nb}$ the position $\boldsymbol{p}^n_{nb}$ and attitude $[\phi, \theta, \psi]$ dynamics can be computed in the NED frame as shown in [27, Chap. 2]:

$$\dot{\boldsymbol{p}}^n_{nb} = \boldsymbol{R}^n_b \boldsymbol{v}^b_{nb} , \tag{26}$$

$$\begin{bmatrix} \dot{\phi} \\ \dot{\theta} \\ \dot{\psi} \end{bmatrix} = \begin{bmatrix} 1 & \sin\phi\tan\theta & \cos\phi\tan\theta \\ 0 & \cos\phi & -\sin\phi \\ 0 & \sin\phi/\cos\theta & \cos/\cos\theta \end{bmatrix} \boldsymbol{\omega}^b_{nb} . \tag{27}$$

The equivalent quaternion-based solution can also be found in [27, Chap. 2].

5. Electric Propulsion System Simulation

In case the motor speed measurement Ω_p is not available, an electric propulsion system model can be used to calculate the speed. Such a model takes the power supply voltage U_b and throttle δ_t as input and outputs the motor acceleration $\dot{\Omega}_p$, reflecting the balance between the generated motor torque Q_m on one side and the load propeller torque Q on the other. Mathematically, a simplified model of these relations can be formulated as follows:

$$U = \delta_t U_b \tag{28}$$

$$I_m = \left(U - \Omega_p K_E\right) R^{-1} \tag{29}$$

$$Q_m = I_m K_E , \tag{30}$$

where U_b is the battery or power supply voltage, U and I_m are the motor voltage and current, R is the electric motor resistance and K_E is the back-emf constant. As mentioned, the balance between the motor torque Q_m and the propeller torque Q drives the acceleration of the motor,

$$\dot{\Omega}_p = \left(Q_m - Q\right) I_p^{-1} , \tag{31}$$

which in simulation is used to compute the motor speed through numeric integration. A more in-depth look at the electric propulsion system modeling can be found in [29, 30].

When analyzing a propulsion system, it is useful to compute both the input and output power. For an electric motor, the input power is given by the electric power formula: $P_{el} = U \cdot I_m$. Conversely, the output power is the mechanical power generated, expressed as $P_m = Q \cdot \Omega_p$. In cases where direct measurements of motor voltage and current are unattainable, the power supplied by the battery $P_b = U_b \cdot I_b$ can serve as a viable approximation for the input power, where the main uncertainty in the approximation arises from power losses in the speed controller.

D. Extraction of the Measured Aerodynamic Forces and Moments

The process of aircraft system identification is greatly simplified when we have access to either the measurements or estimates of the aerodynamic forces and moments. Although not required by the classical OEM, this data allows for a deeper understanding of the model's strengths and weaknesses by enabling individual comparison of the resulting force and moment coefficients. Furthermore, access to the aerodynamic coefficients, as they are presented in Eqs. (35) and (36), makes it possible to use the hybrid OEM described in [32]. In the hybrid OEM, the indirectly measured aerodynamic coefficients are used as weighted outputs, which, in this work, has greatly improved parameter convergence during the system identification process. The rest of this subsection presents the relations necessary to extract these aerodynamic coefficients and perform system identification based on the measurements available in a standard flight log.

The main sensor that allows us to extract the force and moment coefficients from the flight data is the IMU, which normally includes a gyroscope and an accelerometer. The gyroscope measures angular rates $\boldsymbol{\omega}_{nb}^{b} = [p, q, r]^{\top}$, while the accelerometer measures the specific force $\boldsymbol{f}_{nb}^{b} = [a_x, a_y, a_z]^{\top}$, defined as a non-gravitational force per unit mass [27, Chap. 14]. More specifically, it measures the inertial acceleration of the aircraft in the body frame, excluding gravitational acceleration. Mathematically, the accelerometer measurements are related to the total force as follows:

$$m\boldsymbol{f}_{nb}^{b} = \boldsymbol{F}^{b} - \boldsymbol{F}_{gravity}^{b} = \boldsymbol{F}_{aero}^{b} + \boldsymbol{F}_{prop}^{b} \; . \tag{32}$$

By rewriting Eq. (32), the aerodynamic force coefficients can be obtained as a function of the measured accelerations:

$$\begin{bmatrix} C_X \\ C_Y \\ C_Z \end{bmatrix} = \frac{1}{\bar{q}S}\left(m\boldsymbol{f}_{nb}^{b} - \boldsymbol{F}_{prop}^{b}\right) \; . \tag{33}$$

Similarly, by combining Eqs. (22b) and (23b), the aerodynamic moment coefficients can be obtained as a function of the angular rates measured by the gyroscope:

$$\begin{bmatrix} C_l \\ C_m \\ C_n \end{bmatrix} = \frac{1}{\bar{q}S}\begin{bmatrix} \frac{1}{b} \\ \frac{1}{\bar{c}} \\ \frac{1}{b} \end{bmatrix}\left(\boldsymbol{I}\dot{\boldsymbol{\omega}}_{nb}^{b} + \boldsymbol{\omega}_{nb}^{b} \times \boldsymbol{I}\boldsymbol{\omega}_{nb}^{b} - \boldsymbol{M}_{prop,rear}^{b}\right) \; . \tag{34}$$

Eqs. (33) and (34) can also be written out as a system of equations in Eq. (35) [7, Chap. 3].

$$C_X = \frac{(ma_x - T)}{\bar{q}S} \tag{35a}$$

$$C_Y = \frac{ma_y}{\bar{q}S} \tag{35b}$$

$$C_Z = \frac{ma_z}{\bar{q}S} \tag{35c}$$

$$C_l = \frac{1}{\bar{q}Sb}\left[I_x\dot{p} - I_{xz}(pq + \dot{r}) + \left(I_z - I_y\right)qr + Q + I_p\dot{\Omega}_p\right] \tag{35d}$$

$$C_m = \frac{1}{\bar{q}S\bar{c}}\left[I_y\dot{q} + (I_x - I_z)\,pr + I_{xz}\left(p^2 - r^2\right) + I_p\Omega_p r\right] \tag{35e}$$

$$C_n = \frac{1}{\bar{q}Sb}\left[I_z\dot{r} - I_{xz}(\dot{p} - qr) + \left(I_y - I_x\right)pq - I_p\Omega_p q\right] \tag{35f}$$

The transformation from body frame to stability frame follows Eq. (20),

$$\begin{bmatrix} C_D \\ C_Y \\ C_L \end{bmatrix} = \boldsymbol{R}_b^s(\alpha)\begin{bmatrix} -C_X \\ C_Y \\ -C_Z \end{bmatrix} \; . \tag{36}$$

III. Experiment Setup and Data Analysis

This section describes the flight and wind tunnel experiments used to model and identify the Skywalker X8 UAV model. Specifically, the system identification maneuvers and the measured data are described. In addition, an assessment of the measurement uncertainty is presented.

A. Maneuver Design

The choice of maneuver periods and amplitudes was based on transfer function analysis obtained from previous models of the Skywalker X8 UAV [5, 6]. The analysis was performed as part of a master's thesis work by Trondstad [33]. An overview of the maneuvers performed is presented in Table 2, and a visualization of the maneuver types is shown in Fig. 2. The periods specified in Table 2 correspond to the length of a single deflection in the maneuver; for doublets, this means that the period of the excited frequency is twice that period (0.8 s). The *3211*- and *121*-maneuvers excite a range of frequencies with periods two to five times the deflection period, i.e., 0.6-1.2s.

Table 2 Overview of the performed system identification maneuvers.

Direction	Type	Deflection Period	Amplitude	Airspeed	Number of Experiments
Lateral	*121*	0.3 s	15°	18m/s	7
Lateral	doublet	0.4 s	15°	18m/s	5
Longitudinal	*3211*	0.3 s	10°	18m/s	8
Longitudinal	doublet	0.4 s	15°	18m/s	8

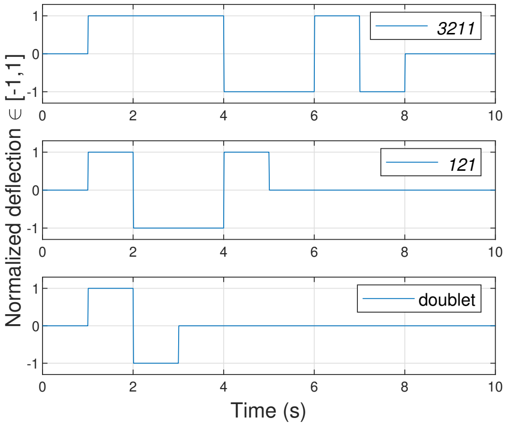

Fig. 2 Overview of the maneuver types. Deflection period is 1 s.

A hard constraint on the maneuver period length is related to the line of sight operation of the UAV. The longest straight part of the trajectory flown by the UAV during testing was about 400 m, allowing for one or two 10-second maneuvers. This makes excitation of the slow dynamic modes, such as the phugoid and spiral diverse modes, challenging, as the corresponding mode periods are often larger than 10 seconds. Consequently, the sum of the maneuver time, the setting time, and the period of steady flight before and after the maneuver can quickly exceed 30 seconds. Due to this limitation, the identified coefficients associated with the slow dynamic modes are expected to have higher uncertainty than the rest of the aerodynamic coefficients.

B. Flight Experiments

The test campaign took place at the Breivika airfield in Agdenes, Norway, in May 2023. The maneuvers were carried out during two 30-minute flights, where the UAV flew in a predetermined flight path as shown in Fig. 3a. The estimated position and attitude data have been validated by recreating the flight path in a 3D animation shown in Fig. 3b.

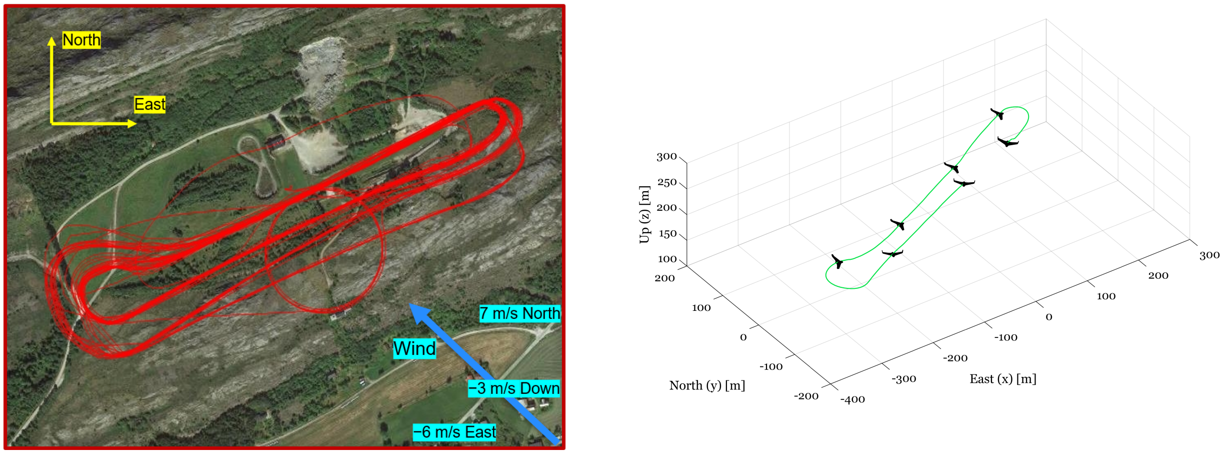

(a) Flight path of the UAV in red. The image was extracted from the ArduPilot Mission Planner software [34]. The time-averaged wind direction in the NED frame is visualized in turquoise.

(b) Animated 3D flight path created using [35].

Fig. 3 Visuzalization of the UAV flight path during the system identifications experiments.

C. Payload and Sensors

The payload and sensors installed on the Skywalker X8 replicate the setup in [36]. The flight stack of the Skywalker X8 is built around the Cube Orange [§] autopilot, which runs on the open-source ArduPilot firmware [¶]. The Cube Orange comprises triple redundant IMUs with magnetometers and pressure sensors. Additionally, the Skywalker X8 has an airspeed sensor, a pitot-static tube, and a global navigation satellite system (GNSS) receiver. Furthermore, the ArduPilot firmware provides state estimates computed using an EKF [37], which includes estimates of the wind vector, the angle of attack, and the sideslip angle.

D. Data Pre-Processing

Resampling and filtering of the data was performed prior to any calculations and transformations described in Section II. More specifically, all measurements and estimates were resampled to a common frequency of 40 Hz set by the ArduPilot EKF. Furthermore, to get angular accelerations, used to compute aerodynamic moments in Eq. (35), numerical differentiation of angular velocities was performed, followed by low-pass filtering to remove noise.

During the flight, a strong wind was estimated by the EKF, indicating a 9 m/s north-west wind, with a 2.8 m/s vertical component. The vertical component was not provided directly by the EKF but was computed during post-processing based on the relative velocity estimates in the horizontal plane and the measured airspeed. To analyze the credibility of the vertical wind estimate, the resulting air data, shown in Fig. 4, was compared to previous Skywalker X8 flight experiments performed with a five-hole air probe [38, Fig. 11]. Based on this comparison, the combination of an angle of attack of 8° at an airspeed of 18 m/s has been deemed credible.

In general, using expensive measurement equipment, such as a five-hole probe, on small low-cost UAVs is quite challenging. Due to the small size, it might be difficult to find an appropriate mounting location for the probe and correct for potential measurement uncertainties caused by mounting errors. Furthermore, for small UAVs, the sensor might be several times more expensive than the platform itself, substantially increasing the financial risk associated with the experiments. Based on previous system identification experience on the same platform [6], and due to the mentioned concerns, we decided to use the air data estimates provided by the ArduPilot EKF instead of flying with the five-hole air probe. Furthermore, results from previous flights with the five-hole probe [38] provide a good reference

---

[§] https://cubepilot.org/

[¶] https://ardupilot.org/

point to validate the current air data estimates. The drawback of using an EKF-estimated angle of attack and sideslip is that these estimates have varying certainty depending on the wind conditions and the complexity of the performed maneuver. This is important to consider when discussing the model prediction results in regions far from the trim point.

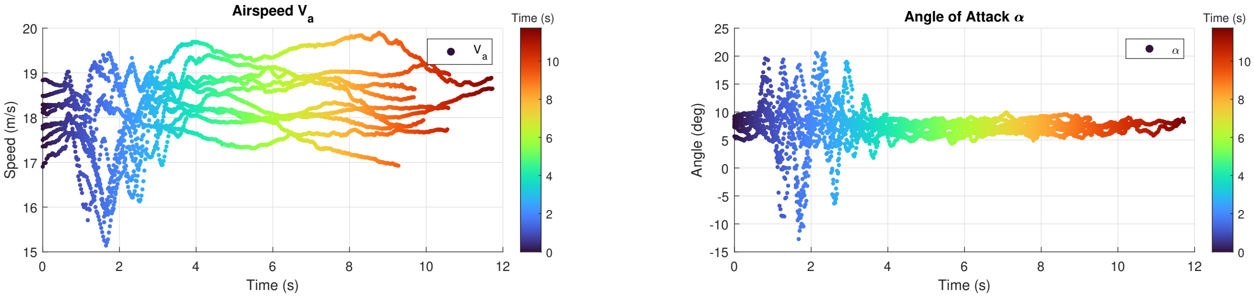

Fig. 4 Measured airspeed V_a and estimated angle of attack α of the Skywalker X8 UAV. The air data is comparable to the flight test results seen in [38] where a five-hole air probe was used to measure α directly.

E. Data Selection

The measured data is initially validated visually, using the drag and lift curves in Fig. 5. First- and second-order polynomials were fitted to the data to showcase the measured mean and the associated confidence intervals. The lift and drag curves exhibit credible trends, yet two points should be discussed in greater detail.

(i) According to the wind tunnels tests, the Skywalker X8 should have a positive lift at $\alpha = 0$ with $C_{L_0} = 0.058$ [6]. However, the flight data in this article indicates a negative lift coefficient at $\alpha = 0$. Although this could be true for the particular Skywalker X8 used in this study, it could also be a result of uncertainties in the vertical wind estimates, which directly affect the computed α Eqs. (15) and (16). On the other hand, as presented earlier, the directly measured air data in [38] is similar to the airspeed and angle of attack presented here, and according to the authors of [6], there were uncertainties related to the selection of the zero angle of attack setting in the wind tunnel. Another relevant input is the elevator deflection; due to a strong vertical wind of -2.8 m/s during the experiments, the UAV was flying with a non-zero elevator deflection, which shifts the whole lift curve down, thus explaining some of the discrepancies between the flight data and the wind tunnel tests.

(ii) There are several data points in Fig. 5a that indicate negative drag values. Negative drag is not physical and can be explained by a combination of uncertainties in the accelerometer measurement, the thrust force compensation done in Eq. (35b), and angle of attack estimates. The unmodeled part of the coupling between the drag and the thrust force could also explain some uncertainty. This is, however, expected when analyzing flight data of a small fixed-wing aircraft such as the Skywalker X8. An aircraft with a relatively large wing area and a small weight of 3.4 kg is highly susceptible to gusts and wind disturbances, which increases the likelihood of encountering aerodynamic states far out of trim.

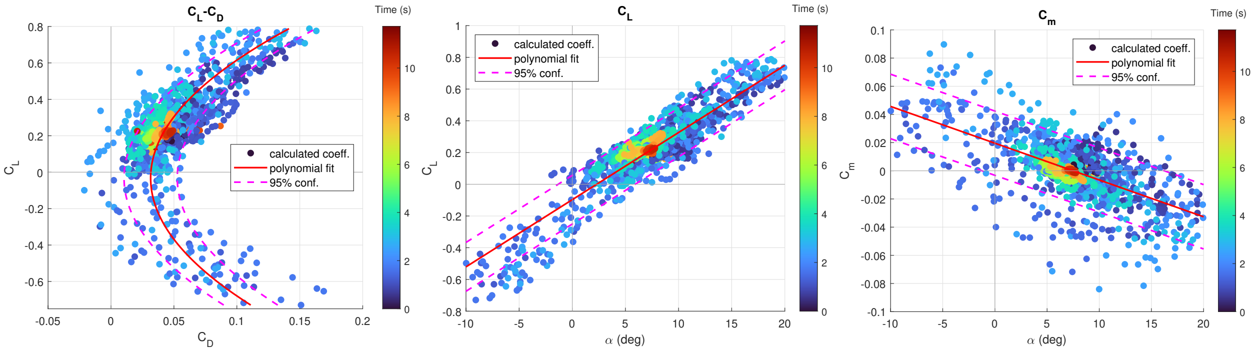

(a) C_L **vs** C_D **(b)** C_L **vs** α **(c)** C_m **vs** α

Fig. 5 Drag, lift, and pitch moment curves computed using data from ten maneuvers at 18 m/s. The coefficients are computed as shown in Eqs. (35) and (36). The color bar is related to time series data in Fig. 4. Focusing on the scatter points in red provides a good indication of the Skwylaker X8's trim condition when flying at 18 m/s.

In total, about 40% of the maneuvers displayed in Table 2 were selected for system identification. The selection process involved analysis of the measured and estimated air data and the analysis of the computed aerodynamic coefficient curves in Fig. 5. The figures employ a coloring scheme based on the temporal state, which has been used to relate the measurement scattering to the aerodynamic state. As expected, the most significant uncertainty in the data coincides with measurements at the last section of the maneuver, i.e., at about three seconds after the maneuver starts (points in light blue color), while the data from the steady state section of the maneuver, in orange and red, has a relatively small spread.

F. Propulsion System Model

The propulsion system of the Skywalker X8 UAV consists of an electric Hacker A40-12S V2 14-pin KV610 motor, a Jeti SPIN Pro 66 speed controller, and a 14x8 Aeronaut CAM folding propeller. The propeller thrust and torque parameters were identified separately based on wind tunnel experiments and are presented in Tables 3 and 4. Parameters related to the motor, i.e., back-emf K_E and electrical resistance R, and the speed controller, were identified using data gathered by Coates et al. in [30].

Table 3 Propeller thrust and torque coefficients used in Eqs. (8) and (9).

C_T		C_Q	
C_{T_0}	0.1400	C_{Q_0}	0.0082
C_{T_1}	-0.0300	C_{Q_1}	0.0112
C_{T_2}	-0.2370	C_{Q_2}	-0.0211
C_{T_3}	0.0847		

Table 4 Propulsion system parameters.

Name	Parameter	Value
Motor back-EMF constnat	k_E	0.0145 V/(rad/s)
Motor resistance	R	0.0907 Ω
Propeller diameter	D	14" or 0.3556 m
Propeller inertia	I_p	3.46×10^{-4} kgm^2

Figure 6 displays measurements alongside model prediction results derived from multistep experiments conducted in a wind tunnel at a constant speed of 18 m/s. The identified model is a propulsion system model that takes power supply voltage and throttle as input and outputs the resulting motor acceleration. The motor acceleration is then integrated to get the motor speed, making it possible to compute propeller thrust and torque, as described in Section II.C.5.

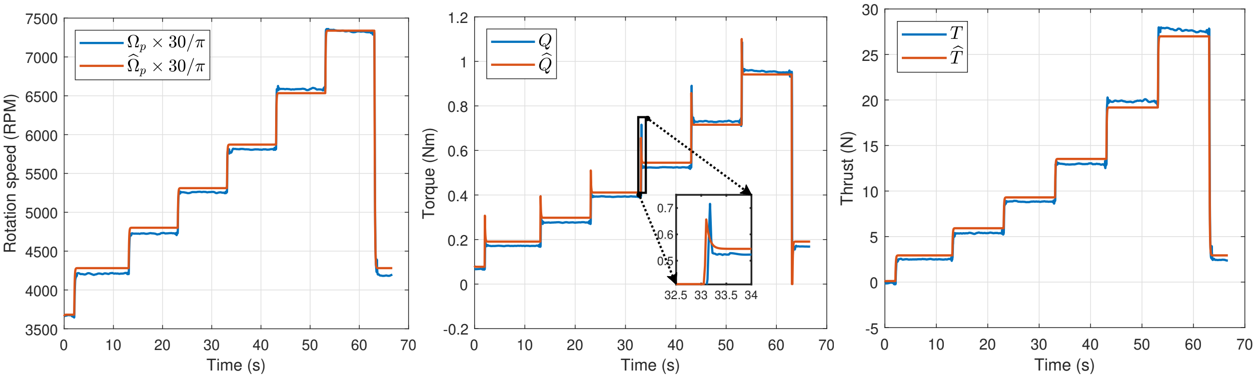

(a) Motor speed model. (b) Propeller torque model. (c) Propeller thrust model.

Fig. 6 Propeller model identified based on multistep experiments performed in a wind tunnel at a constant speed of 18 m/s. The spikes in the torque data (b) are due to the gyroscopic effect generated during acceleration as described in Eq. (11). Model prediction results are indicated by the $\widehat{\ }$. The zoom plot in (b) is made using [39].

Motor speed was not measured during the system identification experiments with the Skywalker X8; the previously described model was therefore used to generate motor speed, propeller torque, and thrust from the measured battery voltage and throttle data. The model output for one of the experiments is shown in Fig. 7. The result can be partially validated by comparing the measured and simulated power usage, i.e., P_b and $\widehat{P}_{el}$ in Fig. 7a.

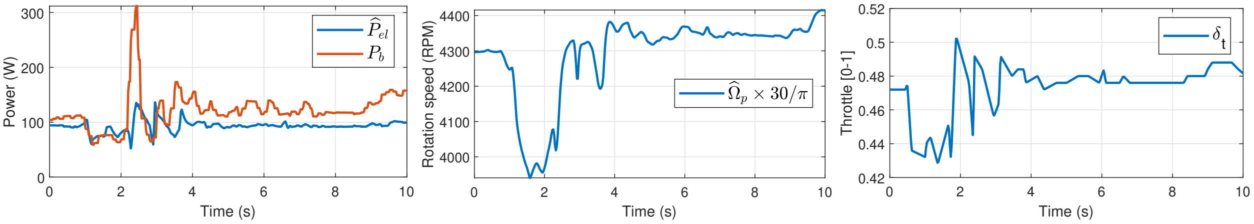

(a) Electrical power. **(b) Motor speed.** **(c) Propeller throttle.**

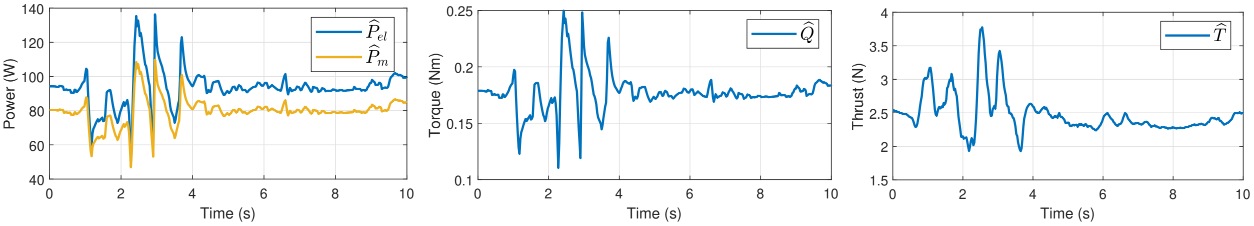

(d) Electrical and mechanical power. **(e) Propeller torque.** **(f) Propeller thrust.**

Fig. 7 Output of the propulsion system model used as input to the system identification for the Skywalker X8 UAV. The throttle and battery power calculated from the measured voltage and current are available from flight experiments. The rest of the propulsion system data is generated by the identified model in Tables 3 and 4. Electrical power in (d) is computed as motor voltage times motor current, and the mechanical power is computed as motor torque times motor speed. The ratio describes the motor efficiency, which is about 85% in this case.

IV. Results

This section presents the aerodynamic modeling results for the Skywalker X8 UAV identified at 18 m/s airspeed.

A. Model Fitting Results

The initial attempts at system identification followed the classic OEM, with coefficients from [5] as the starting point. However, after experiencing slow parameter convergence, the hybrid OEM described in [32] was tested. In hybrid OEM, indirectly measured aerodynamic coefficients can be used as weighted outputs. Implementing this change significantly improved the parameter convergence rate, enabling the identification of the final model presented here. Thus, the hybrid OEM method was used to estimate the 28 aerodynamic parameters of the nonlinear model in Eqs. (17) and (18) by fitting the model outputs to the measured experimental data and the computed aerodynamic coefficients.

The system identification was based on five longitudinal maneuvers and five lateral maneuvers. Estimation was performed separately for the longitudinal and lateral parameters, while the ten selected maneuvers were kept the same. The parameters and weighted output pairings are shown in Table 5.

Table 5 The table shows the aerodynamic parameters and the weighted outputs used to estimate these parameters. The weighted outputs are grouped for readability. The force and moment coefficients are computed from the state variables as shown in Eqs. (35) and (36).

Input data (ten maneuvers)	Parameters	Weighted outputs	Parameters	Weighted outputs
3 x longitudinal *3211* 2 x longitudinal doublet 3 x lateral *121* 2 x lateral doublet	$C_{D_{(*)}}$ $C_{L_{(*)}}$ $C_{m_{(*)}}$	z, θ	$C_{Y_{(*)}}$ $C_{l_{(*)}}$ $C_{n_{(*)}}$	z, ϕ, ψ
		u, w, q		v, p, r
		a_x, a_z		a_y
		V_a, α		V_a, β
		C_D, C_L, C_m		C_Y, C_l, C_n

1. Nonlinear Model Prediction Analysis

The model prediction results for a longitudinal *3211*- and a lateral doublet maneuver are presented in Figs. 8 and 9. Evaluation of the model predictions can be split into two stages: (i) prediction of the aerodynamic forces and moments, and (ii) prediction of the aircraft motion. Forces and moments are easier to model and identify as direct measurements of aircraft acceleration and angular rates are available from the IMU. In contrast, the motion of the aircraft is based on an EKF, which combines the airspeed, IMU, and GNSS data to estimate the wind and the aerodynamic state of the aircraft, making the model prediction analysis more convoluted.

(i) A look at the model prediction results for both lateral and longitudinal examples reveals that the model can predict the force and moment coefficients for the duration of the recorded maneuvers. In general, the model is able to replicate large dynamic movements with high accuracy; however, the prediction of the low amplitude dynamics is not as accurate. This is an expected result, as the measurement noise and environmental disturbances are difficult to replicate in simulation. When analyzing the individual force and moment coefficients, it is noticeable that the predicted drag peaks deviate from the measurement in Fig. 8; however, as already discussed, modeling the drag can be challenging due to the coupling effects between the propulsion model and the airframe drag. Identification of an aero-propulsive model as suggested in [24] or a more in-depth modeling of the thrust compensation in Eq. (35b) can potentially be used to improve this modeling error.

(ii) The second stage results provide reasonably good predictions as well, especially for the angle of attack shown in Fig. 8. This is expected as α is directly related to the longitudinal force and moment coefficients. When it comes to the altitude, heading angle, and body frame speeds, the model predictions are less accurate. It should be noted that the wind makes the estimation and prediction problem much more challenging. Calm wind conditions should, therefore, be prioritized to a higher degree when performing system identification maneuvers with small aircraft. Alternatively, direct measurements of the α and β should be considered.

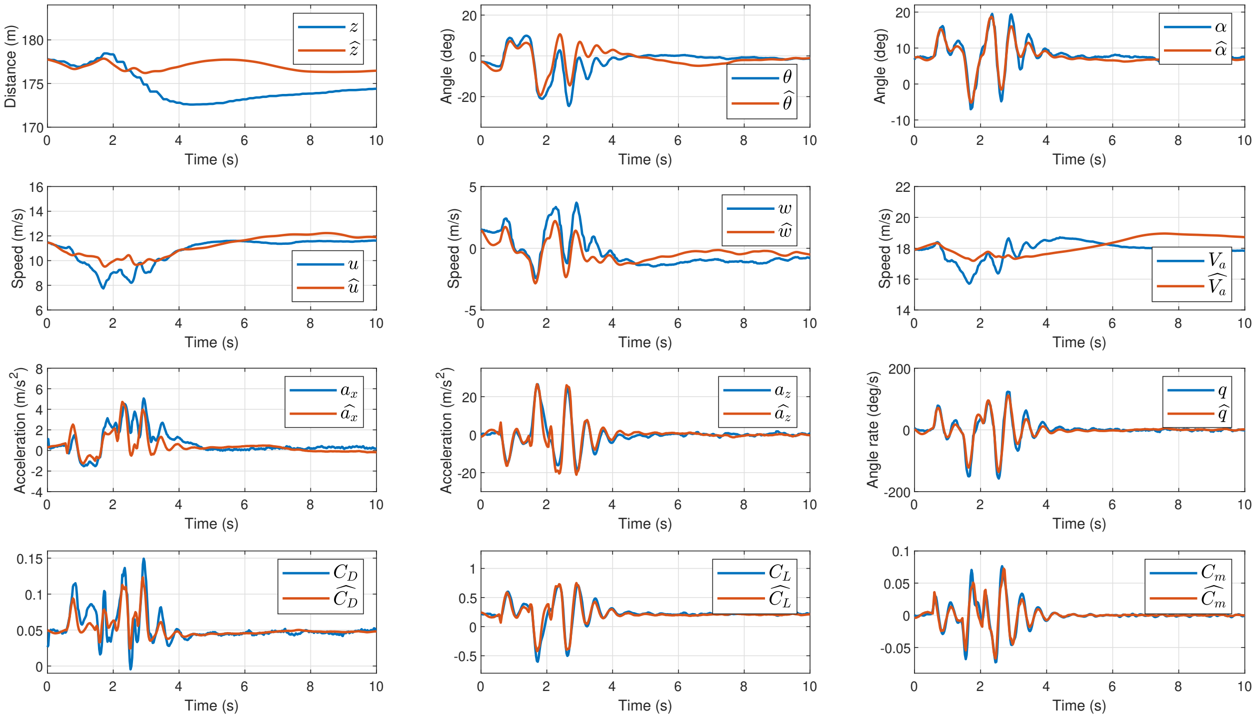

Fig. 8 Weighted outputs and the model prediction results for a longitudinal *3211*-maneuver used in the identification of longitudinal parameters $C_{D_{(*)}}, C_{L_{(*)}}, C_{m_{(*)}}$. The predictions are indicated by the $\widehat{\ }$.

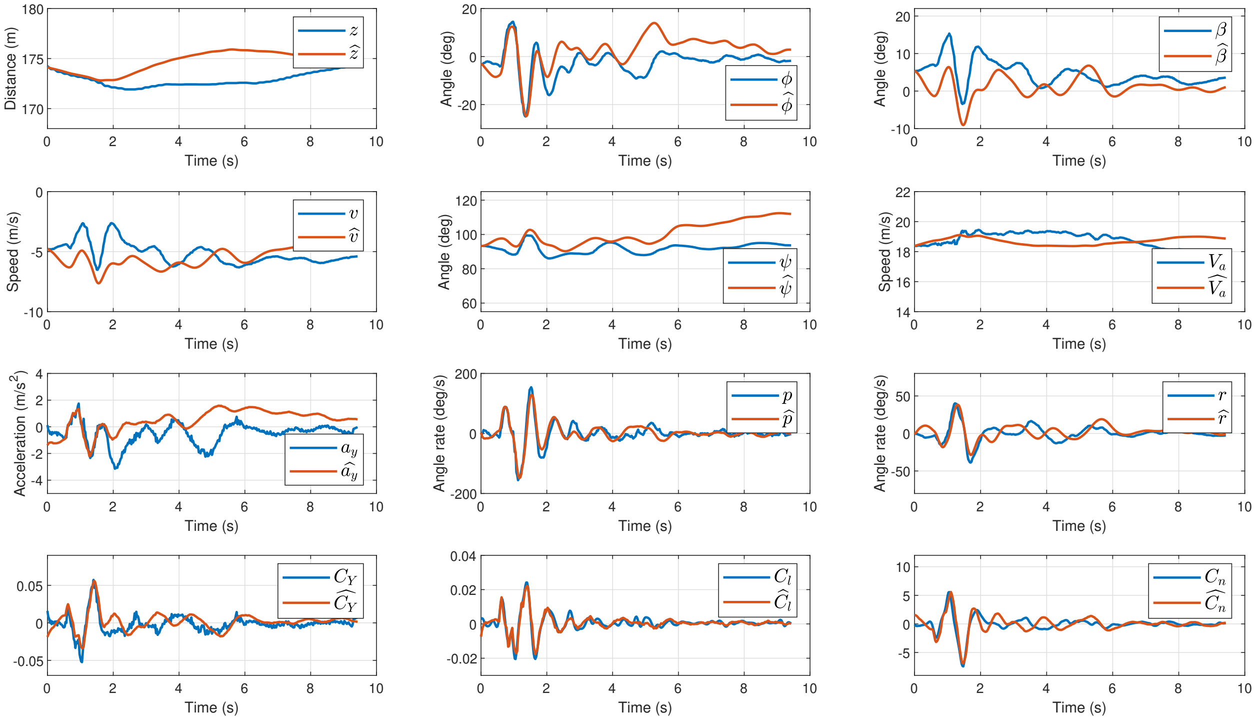

Fig. 9 Weighted outputs and the model prediction results for a lateral doublet maneuver used in the identification of lateral parameters $C_{Y_{(*)}}, C_{l_{(*)}}, C_{n_{(*)}}$. The predictions are indicated by the $\widehat{\ }$.

Figure 10 provides an additional way of analyzing the identified model by comparing the drag, lift, and pitch moment curves from the flight data with the curves generated by the model. Although the presented scatter plot doesn't indicate the model's accuracy, it can provide a general understanding of the model's region of validity and distribution of the measured data points. Visual analysis indicates a good model fit about the trim, indicated by the dense regions of the scatter plot. In the regions further away from the trim, the model prediction accuracy is diminished; this is especially visible for values at the negative angles of attack, where only limited amounts of data have been collected. It is, therefore, important to be aware of the model's region of validity and its inherent limitations when extrapolating further model-based results.

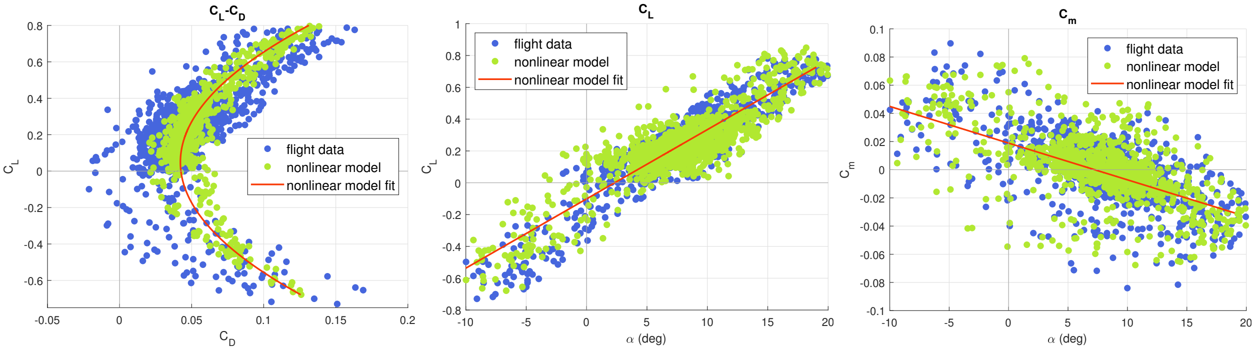

(a) C_L **vs** C_D **(b)** C_L **vs** α **(c)** C_m **vs** α

Fig. 10 Comparison of drag, lift, and pitch moment curves based on flight data and simulation of ten maneuvers at 18 m/s. The red line shows the model mean for the ten maneuvers computed by fitting a polynomial to the output data.

2. Identified Model Parameters

The identified parameters are presented in Table 6. The coefficient and standard deviation values (StdDev.) were obtained using the Fitlab tool [16]. The model structure was identified through stepwise regression [7, Chap. 5], where regressors are gradually added to the model and several statistics, such as model prediction error, are analyzed to keep or ignore a particular regressor. The low standard deviations in Table 6 indicate a good alignment between the data and the selected model structure. Furthermore, during the system identification process, none of the coefficients had a correlation of more than 0.9, which is a standard cutoff criterion for pairwise regressor correlation [7, Chap. 5].

Analysis of Table 6, or equivalently Eqs. (17) and (18), shows that the identified model is for the most part linear, except for the drag, which is modeled as a second-order function of lift and includes a propeller thrust component. The negative thrust component indicates that the drag decreases with increased throttle, i.e., the propeller has an impact on the flow across the airframe.

Table 6 Ideintifed coefficients of the nonlinear aerodynamic model given by Eqs. (17) and (18). The coefficients were identified according to Table 5, based on flight maneuvers performed at the speed of 18 m/s. The (Rel. %) column shows the standard deviation as a percentage of the coefficient value.

C_L			C_D			C_m		
Param.	**Value**	**StdDev. (Rel. %)**	**Param.**	**Value**	**StdDev. (Rel. %)**	**Param.**	**Value**	**StdDev. (Rel. %)**
C_{L_0}	-0.047	3.11e-03 (5.3)	C_{D_0}	0.058	6.19e-04 (1.3)	C_{m_0}	0.023	2.70e-04 (1.1)
C_{L_α}	2.480	2.35e-02 (0.9)	C_{D_q}	0.935	4.99e-02 (7.2)	C_{m_α}	-0.257	1.76e-03 (0.7)
C_{L_q}	20.576	2.72e-01 (1.4)	$C_{D_{C_T}}$	-0.399	1.79e-02 (13.1)	C_{m_q}	-1.618	2.64e-02 (1.8)
$C_{L_{\delta_e}}$	1.558	2.05e-02 (1.3)	$C_{D_{k1}}$	-0.035	1.91e-03 (9.0)	$C_{m_{\delta_e}}$	-0.270	1.78e-03 (0.7)
			$C_{D_{k2}}$	0.161	2.17e-03 (1.4)			
C_Y			C_l			C_n		
Param.	**Value**	**StdDev. (Rel. %)**	**Param.**	**Value**	**StdDev. (Rel. %)**	**Param.**	**Value**	**StdDev. (Rel. %)**
C_{Y_0}	0.010	2.45e-04 (2.5)	C_{l_0}	0.006	8.41e-05 (1.4)	C_{n_0}	-4.7e-04	1.16e-05 (2.4)
C_{Y_β}	-0.272	4.21e-03 (1.6)	C_{l_β}	-0.106	1.28e-03 (1.2)	C_{n_β}	0.019	2.26e-04 (1.2)
C_{Y_p}	-0.251	1.24e-02 (5.0)	C_{l_p}	-0.316	4.03e-03 (1.3)	C_{n_p}	-0.011	7.86e-04 (7.0)
C_{Y_r}	0.186	1.69e-02 (8.9)	C_{l_r}	0.068	4.36e-03 (6.4)	C_{n_r}	-0.060	6.43e-04 (1.1)
$C_{Y_{\delta_a}}$	0.094	3.42e-03 (3.6)	$C_{l_{\delta_a}}$	0.101	1.08e-03 (1.1)	$C_{n_{\delta_a}}$	-0.007	2.15e-04 (3.1)

3. Actuators

In addition to the aerodynamic model, two actuator models had to be implemented to obtain a complete simulation-ready model of the Skywalker X8 UAV. Following [5], a second-order process was used to model the elevon dynamics and a first-order process was used to model the throttle input. Both models include input delays, identified by matching control inputs to the measured IMU data, i.e., the time from a change in a control signal to a change in the measured acceleration or angular rate. The complete set of actuator model parameters is listed in Table 7.

Table 7 Actuator model parameters for a 2nd order servo system controlling the elevons and a 1st order system for the throttle control.

Servo 2nd order system			Throttle 1st order system	
Natural frequency	**Damping**	**Input delay**	**Time constant**	**Input delay**
100 rad/s	0.707	0.07 s	0.2 s	0.05 s

V. Conclusion

The aim of the paper is to address the need for accurate models to enable simulation-based testing and rapid development of applications tailored to small fixed-wing UAVs. To meet this goal, our paper presents a complete nonlinear aerodynamic model of the Skywalker X8 platform, including the propulsion system and the control surface actuator models. In general, the model provides a good match with the measured flight data for the large dynamic maneuvers. At the same time, the predictions near the steady state are naturally not as accurate due to the measurement noise and wind gusts encountered during the experiments.

This paper has examined several critical factors that influence the system identification of small fixed-wing UAV models. Here, we revisit these key insights and challenges.

- The hybrid output error method: The nonlinear model presented in this article was identified using the hybrid OEM, which, in contrast to the classical OEM, uses the constructed force and moment coefficient in addition to the directly measured data as weighted outputs. In this case study with Skywalker X8 UAV, the classical OEM didn't work due to slow parameter convergence. Thus, the use of the force and moment coefficients as weighted outputs was critical to obtaining a good model.
- Wind susceptibility of small UAVs: Small, lightweight UAVs exhibit heigh sensitivity to wind disturbances. Unlike larger aircraft, which act as low-pass filters, these agile platforms are affected significantly by wind gusts, making the model identification process challenging. It is, therefore, important to ensure that the flight experiments are performed in calm wind conditions. Alternatively, direct measurement of the air data should be considered. The latter option might, however, be challenging due to sensor costs and mounting space limitations on a small fixed-wing UAVs.
- Drag modeling: Accurately modeling the aerodynamic drag remains challenging due to the aero-propulsive coupling. A way to decouple these effects is by performing specific maneuvers, e.g., a gliding maneuver where the motor can be turned off, and the aerodynamic drag can be measured without the propulsive effects. As mentioned previously, this type of test is difficult to perform due to line-of-sight limitations and regulations regarding the flight altitude. In this article, the drag model uncertainty is partially mitigated by identifying an accurate propulsion system model based on wind tunnel experiments, ensuring that the thrust force compensation introduces minimal error. Another approach is presented in [24], where the aero-propulsive model is not decoupled and modeled as one.
- Modeling asumptions: The lateral-longitudinal dynamics are decoupled in the identified nonlinear model. The decoupling choice was based on stepwise regression results and a simplification assumption, the validity of which was affirmed based on the model prediction results. However, since the model prediction results are imperfect, some prediction errors can be attributed to the unmodelled coupling effects. For instance, aerodynamic drag is often modeled as a function of the sideslip angle, which is not done in this paper.
- Region of validity: Aircraft dynamics are highly nonlinear; this means that the accuracy of a model identified at a specific airspeed will deteriorate quickly for states far outside the trim condition at that airspeed. This has to do with Reynolds number effects, turbulent flow, and flow separation. In this paper, a clear decrease in model accuracy can be observed for negative angles of attack, where the modeled lift and drag start to deviate from the measurements.

Next Steps

Based on the insights from the work presented in this article, several possibilities for future work emerge:

- Linearization and aerodynamic mode analysis: Linearizing the identified nonlinear model into lateral and longitudinal state-space representations can enhance our understanding of the aircraft's dynamics around specific trim points. Linear models facilitate frequency domain analysis, enabling the identification of aerodynamic modes. This analysis is crucial for various applications, including control system design, stability assessment, and efficient simulation. Furthermore, it provides an additional description of the model for validation against similar research, ensuring greater reliability of the modeling results.
- In-depth model analysis: A comprehensive examination of the identified model, including investigationg of the aerodynamic coupling and residual distribution analysis, can improve the model accuracy assessment.
- Model extension to different airspeeds: A way to increase the region of validity of the model is to identify a set of models across varying airspeeds and merge them into a unified model —a result that can provide substantial value for simulation-based testing and development of UAVs.
- Comparative study of model prediction results: In-depth performance comparison of nonlinear and linearized models against simulated flight data can offer further insights into the validity and limitations of linear approximations.

Acknowledgments

The work is sponsored by the Research Council of Norway through the IKTPLUSS project with number 316425.

The authors thank NTNU UAV lab, especially Pål Kvaløy, Dr. Artur Zolich, and Dr. Kristoffer Gryte, for providing access to the Skwyalker X8 UAV, organizing the flight experiments, and performing the flights. Additionally, we thank Dr. Haiyang Chao for the great discussions about system identification during his visit to NTNU in Trondheim. Lastly, we acknowledge the contribution of Phillip Tronstad, who helped design and perform the flight experiments as part of his master's thesis work.

References

[1] Federal Aviation Administration, "FAA Aerospace Forecast FY 2023-2043," USA, 2023. URL https://www.faa.gov/dataresearch/aviation/aerospaceforecasts/faa-aerospace-forecast-fy-2023-2043, accessed Aug. 11, 2023.

[2] Shakhatreh, H., Sawalmeh, A. H., Al-Fuqaha, A., Dou, Z., Almaita, E., Khalil, I., Othman, N. S., Khreishah, A., and Guizani, M., "Unmanned Aerial Vehicles (UAVs): A Survey on Civil Applications and Key Research Challenges," *IEEE Access*, Vol. 7, 2019, pp. 48572–48634. https://doi.org/10.1109/ACCESS.2019.2909530.

[3] Gao, M., Hugenholtz, C. H., Fox, T. A., Kucharczyk, M., Barchyn, T. E., and Nesbit, P. R., "Weather constraints on global drone flyability," *Scientific Reports*, Vol. 11, No. 1, 2021. https://doi.org/10.1038/s41598-021-91325-w.

[4] Hann, R., and Johansen, T. A., "Unsettled Topics in Unmanned Aerial Vehicle Icing," Tech. rep., SAE Technical Paper, 2020. https://doi.org/10.4271/EPR2020008.

[5] Gryte, K., Hann, R., Alam, M., Roháč, J., Johansen, T. A., and Fossen, T. I., "Aerodynamic modeling of the skywalker x8 fixed-wing unmanned aerial vehicle," *2018 International Conference on Unmanned Aircraft Systems (ICUAS)*, IEEE, 2018, pp. 826–835. https://doi.org/10.1109/icuas.2018.8453370.

[6] Reinhardt, D., Gryte, K., and Johansen, T. A., "Modeling of the Skywalker X8 Fixed-Wing UAV: Flight Tests and System Identification," *2022 International Conference on Unmanned Aircraft Systems (ICUAS)*, IEEE, 2022, pp. 506–515. https://doi.org/10.1109/icuas54217.2022.9836104.

[7] Morelli, E. A., and Klein, V., *Aircraft system identification: theory and practice*, 2$^{\text{nd}}$ ed., Sunflyte Enterprises, Williamsburg, VA, 2016.

[8] Jategaonkar, R. V., *Flight vehicle system identification: A time domain methodology*, 2$^{\text{nd}}$ ed., American Institute of Aeronautics and Astronautics, 2015. https://doi.org/10.2514/4.102790.

[9] Lindner, M., Wallisch, J., and Hann, R., "UAV Icing: Numerical Simulation of Icing Effects on Wing and Empennage," Tech. rep., SAE Technical Paper, 2023. https://doi.org/10.4271/2023-01-1384.

[10] Hann, R., Hearst, R. J., Sætran, L. R., and Bracchi, T., "Experimental and Numerical Icing Penalties of an S826 Airfoil at Low Reynolds Numbers," *Aerospace*, Vol. 7, No. 4, 2020. https://doi.org/10.3390/aerospace7040046.

[11] Fajt, N., Hann, R., and Lutz, T., "The influence of meteorological conditions on the icing performance penalties on a UAV airfoil," *8th European Conference for Aeronautics and Space Sciences (EUCASS)*, 2019. https://doi.org/10.13009/EUCASS2019-240.

[12] Deiler, C., "Aerodynamic modeling, system identification, and analysis of iced aircraft configurations," *Journal of Aircraft*, Vol. 55, No. 1, 2018, pp. 145–161. https://doi.org/10.2514/1.C034390.

[13] Deiler, C., Ohme, P., Raab, C., Mendonca, C., and Silva, D., "Facing the challenges of supercooled large droplet icing: Results of a flight test based joint DLR-embraer research project," *SAE International Journal of Advances and Current Practices in Mobility*, Vol. 2, No. 2019-01-1988, 2019, pp. 192–204. https://doi.org/10.4271/2019-01-1988.

[14] Deiler, C., "Comparison of flight characteristics of two different airplanes and ice configurations," *Journal of Aircraft*, Vol. 57, No. 5, 2020, pp. 995–1000. https://doi.org/10.2514/1.C035801.

[15] Deiler, C., "Flight Characteristics with Different Supercooled Large Droplet Ice Configurations," *The Aeronautical Journal*, Vol. 126, No. 1299, 2022, pp. 848–865. https://doi.org/10.1017/aer.2021.98.

[16] Deiler, C., Mönnich, W., Seher-Weiß, S., and Wartmann, J., "Retrospective and Recent Examples of Aircraft and Rotorcraft System Identification at DLR," *Journal of Aircraft*, 2023, pp. 1–27. https://doi.org/10.2514/1.C037262.

[17] Dorobantu, A., Murch, A., Mettler, B., and Balas, G., "System identification for small, low-cost, fixed-wing unmanned aircraft," *Journal of Aircraft*, Vol. 50, No. 4, 2013, pp. 1117–1130. https://doi.org/10.2514/1.C032065.

[18] Arifianto, O., and Farhood, M., “Development and modeling of a low-cost unmanned aerial vehicle research platform,” *Journal of Intelligent & Robotic Systems*, Vol. 80, 2015, pp. 139–164. https://doi.org/10.1007/s10846-014-0145-3.

[19] Grymin, D. J., and Farhood, M., “Two-step system identification and trajectory tracking control of a small fixed-wing UAV,” *Journal of Intelligent & Robotic Systems*, Vol. 83, 2016, pp. 105–131. https://doi.org/10.1007/s10846-015-0298-8.

[20] Venkataraman, R., and Seiler, P., “System identification for a small, rudderless, fixed-wing unmanned aircraft,” *Journal of Aircraft*, Vol. 56, No. 3, 2019, pp. 1126–1134. https://doi.org/10.2514/1.C035141.

[21] Chao, H., Flanagan, H. P., Tian, P., and Hagerott, S. G., “Flight test investigation of stall/spin detection techniques for a flying wing UAS,” *AIAA Atmospheric Flight Mechanics Conference, 2017*, 2017. https://doi.org/10.2514/6.2017-1631.

[22] Tian, P., Chao, H., Flanagan, H. P., Hagerott, S. G., and Gu, Y., “Design and evaluation of UAV flow angle estimation filters,” *IEEE Transactions on Aerospace and Electronic Systems*, Vol. 55, 2019, pp. 371–383. https://doi.org/10.1109/TAES.2018.2852359.

[23] Simmons, B. M., McClelland, H. G., and Woolsey, C. A., “Nonlinear model identification methodology for small, fixed-wing, unmanned aircraft,” *Journal of Aircraft*, Vol. 56, No. 3, 2019, pp. 1056–1067. https://doi.org/10.2514/1.C035160.

[24] Simmons, B. M., Gresham, J. L., and Woolsey, C. A., “Flight-Test System Identification Techniques and Applications for Small, Low-Cost, Fixed-Wing Aircraft,” *Journal of Aircraft*, 2023, pp. 1–19. https://doi.org/10.2514/1.C037260.

[25] Matt, J. J., Hagerott, S. G., Svoboda, B. C., Flanagan, H. P., and Chao, H., “Frequency Domain System Identification of a Small Flying-Wing UAS,” *AIAA Science and Technology Forum and Exposition, AIAA SciTech Forum 2022*, 2022. https://doi.org/10.2514/6.2022-2407.

[26] Matt, J., Chao, H., Shawon, M. H., and Hagerott, S. G., “Longitudinal System Identification for a Small Flying-wing UAS,” *AIAA SciTech Forum 2023*, American Institute of Aeronautics and Astronautics, 2023. https://doi.org/10.2514/6.2023-0628.

[27] Fossen, T. I., *Handbook of Marine Craft Hydrodynamics and Motion Control*, 2$^{\text{nd}}$ ed., John Wiley & Sons Ltd., 2021.

[28] Beard, R. W., and McLain, T. W., *Small Unmanned Aircraft: Theory and Practice*, Princeton University Press, 2012.

[29] Løw-Hansen, B., Müller, N. C., Coates, E. M., Johansen, T. A., and Hann, R., “Identification of an Electric UAV Propulsion System in Icing Conditions,” Tech. rep., SAE Technical Paper, 2023. https://doi.org/10.4271/2023-01-1378.

[30] Coates, E. M., Wenz, A., Gryte, K., and Johansen, T. A., “Propulsion system modeling for small fixed-wing UAVs,” *2019 International Conference on Unmanned Aircraft Systems (ICUAS)*, Institute of Electrical and Electronics Engineers Inc., 2019, pp. 748–757. https://doi.org/10.1109/icuas.2019.8798082.

[31] Simmons, B. M., “System Identification for Propellers at High Incidence Angles,” *Journal of Aircraft*, Vol. 58, No. 6, 2021, pp. 1336–1350. https://doi.org/10.2514/1.C036329.

[32] Özger, E., “Introducing a combined equation/output error approach in parameter estimation,” *48th AIAA Aerospace Sciences Meeting Including the New Horizons Forum and Aerospace Exposition*, 2010. https://doi.org/10.2514/6.2010-34.

[33] Tronstad, P. L., “Model-Based In-Flight Icing Detection for Fixed-Wing UAVs,” Master’s thesis, NTNU, 2023. URL https://ntnuopen.ntnu.no/ntnu-xmlui/handle/11250/3100357, accessed June 2, 2023.

[34] Team, ArduPilot Dev, “Mission planner,” , 2023. URL https://ardupilot.org/planner/, accessed Aug. 11, 2023.

[35] Bużantowicz, W., “Matlab script for 3D visualization of missile and air target trajectories,” *International Journal of Computer and Information Technology*, Vol. 5, 2016, pp. 419–422. URL https://www.ijcit.com/archives/volume5/issue5/Paper050501.pdf, accessed Feb. 1, 2023.

[36] Coates, E. M., Reinhardt, D., Gryte, K., and Johansen, T. A., “Toward Nonlinear Flight Control for Fixed-Wing UAVs: System Architecture, Field Experiments, and Lessons Learned,” *2022 International Conference on Unmanned Aircraft Systems (ICUAS)*, 2022, pp. 724–734. https://doi.org/10.1109/icuas54217.2022.9836064.

[37] Team, ArduPilot Dev, “Extended Kalman Filter (EKF),” , 2023. URL https://ardupilot.org/copter/docs/common-apm-navigation-extended-kalman-filter-overview.html, accessed May 10, 2024.

[38] Borup, K. T., Fossen, T. I., and Johansen, T. A., “A machine learning approach for estimating air data parameters of small fixed-wing UAVs using distributed pressure sensors,” *IEEE Transactions on Aerospace and Electronic Systems*, Vol. 56, No. 3, 2019, pp. 2157–2173. https://doi.org/10.1109/TAES.2019.2945383.

[39] Qiu, K., “ZoomPlot,” , 2024. URL https://github.com/iqiukp/ZoomPlot-MATLAB/releases/tag/v1.5.1, accessed Feb. 1, 2024.